Molecular Determinants of μ-Conotoxin KIIIA interaction with the Voltage-Gated Sodium Channel Nav1.7

Ian H. Kimball[1,*], Phuong T. Nguyen[1,*], Baldomero M. Olivera[2], Jon T. Sack[1,‡], Vladimir Yarov-Yarovoy[1,‡]

[1]Department of Physiology and Membrane Biology, UC Davis, Davis, CA, USA,

[2]Department of Biology, University of Utah, Salt Lake City, UT, USA

* - these authors contributed equally to this work

‡ corresponding authors

Abstract

The voltage-gated sodium (Nav) channel subtype Nav1.7 plays a critical role in pain signaling, making it an important drug target. A number of peptide toxins from cone snails (conotoxins) bind to the extracellular vestibule of the Nav channel pore and block ion conduction. While the known conotoxins have variable selectivity among Nav channel subtypes, they form potential scaffolds for engineering of selective and potent channel inhibitors. Here we studied the molecular interactions between μ-conotoxin KIIIA (KIIIA) and the human Nav1.7 channel (hNav1.7). Using the cryo-electron microscopy (cryo-EM) structure of the electric eel Nav1.4 channel as a template we developed a structural model of hNav1.7 with Rosetta computational modeling. We performed *in silico* docking of KIIIA using RosettaDock and identified residues forming specific pairwise contacts between KIIIA and hNav1.7. Pairwise interactions were experimentally validated using mutant cycle analysis. Comparison with a recently published cryo-EM structure of the KIIIA-hNav1.2 channel complex revealed key similarities and differences between channel subtypes with potential implications for the molecular mechanism of toxin block. Our integrative approach, combining high-resolution structural data with computational modeling and experimental validation, will be useful for engineering of molecular probes to study Nav channels function and for rational design of novel biologics to treat chronic pain, cardiac arrhythmias, and epilepsy.

Introduction

Voltage-gated sodium (Nav) channels play a key role in the action potential generation in excitable cells (1, 2). The nine subtypes of Nav channel α-subunits (named 1.1-1.9) are differentially expressed throughout tissues, and are studied as potential targets for development of therapeutics for chronic pain, cardiac arrhythmias, and epilepsy (3). Human Nav1.7 (hNav1.7) is known to be important for pain signaling and its mutations have been linked to severe pain disorders ranging from complete lack of pain sensation to extreme sensitivity to pain (4-6). Clinical use of local anesthetic drugs is limited because they bind to highly conserved receptor site within the Nav channel pore lumen (7-10).

Nav channels are common targets of small disulfide-knotted peptide toxins from cone snails (conotoxins) (2), which target the extracellular vestibule of the Nav channel pore and offer useful peptide scaffolds for rational design of novel peptide-based therapeutics to treat pain, arrhythmias, and epilepsy (11, 12). μ-conotoxin KIIIA (KIIIA) is a 16 amino acid peptide that potently inhibits TTX-sensitive Nav channels (2, 13, 14), and has shown analgesic properties in animal models of pain (13) (Figure 1A). KIIIA has variable degrees of affinity and block for the different Nav channel subtypes, with 5 nM affinity for rat Nav1.2, 37 nM for r at Nav1.4, and 97 nM for hNav1.7 (2, 13, 15). Structure-activity relationship studies have identified the KIIIA residues K7, W8, R10, D11, H12 and R14 as key for binding to various Nav channel subtypes (13, 15). Specifically, K7, R10 and R14 have been shown to contribute to binding affinity and block of hNav1.7 (15). Interestingly, the relative contribution of KIIIA residues in binding to Nav channels vary between channel subtypes. For example, substitution R14A in KIIIA reduces the affinity for Nav1.2 and Nav1.4 by two orders of magnitude, while only reducing the affinity for Nav1.7 by a 5-fold (15). Substitution R10A in KIIIA similarly shows reduced effect on affinity for Nav1.7 compared to Nav1.2 and Nav1.4, while having a more drastic effect on channel block of Nav1.7 (15). In addition, KIIIA blocks Nav channels incompletely and can co-bind with tetrodotoxin (TTX) to TTX-sensitive Nav channels, while other μ-conotoxins such as GIIIA, GIIIB, and PIIIA block Nav channels completely (16).

Previous studies identified the importance of Nav channel residues near the selectivity filter on the P2-helix in domain III (DIII) for their apparent coupling to residues R10 and R14 on KIIIA (15). Notably, the P2-helix in DIII of hNav1.7 has Threonine at position 1398 and an Isoleucine at position 1399, while all other human Nav channels have Methionine and Aspartate at the corresponding positions (15). These residues were proposed to play a role in the selectivity of KIIIA binding to Nav1.2 and Nav1.4 versus to Nav1.7 (15). Molecular modeling of KIIIA binding to rNav1.4 using restraints from experimental data also revealed contacts between KIIIA and the P2-helix in DIII (17). However, these studies have not provided an explanation for the significant effect of the KIIIA mutations H12A, W8A and D11A on toxin affinity. In this study, we used computational and experimental approaches to investigate the molecular mechanism of the KIIIA interaction with hNav1.7. We present a structural model of KIIIA binding to the hNav1.7 channel based on the eukaryotic electric eel Nav1.4 cryo-EM structure. Our model revealed asymmetric binding of KIIIA to hNav1.7 at the interface between the P2-helices in domain II (DII) and DIII, which exposed a partially open ion conduction pathway that may explain the incomplete blocking characteristic of the toxin. We identified several unique contacts between KIIIA and extracellular loops on hNav1.7, providing key structural insights into binding specificity for different Nav channels subtypes. We used mutant cycle analysis to validate representative pairwise contacts between specific KIIIA and hNav1.7 residues identified from our structural model of the KIIIA –

hNav1.7 complex. Remarkably, the recently published cryo-EM structure of KIIIA - hNav1.2 complex (18) agrees with findings from our computational modeling and functional study. The high atomic accuracy of peptide toxin – Nav channel interactions modeling with Rosetta in combination with functional testing paves the way for the rational design of novel selective inhibitors targeting Nav channels with high selectivity and potency.

Results

Molecular modeling reveals asymmetric binding of KIIIA to hNav1.7 pore

To characterize the molecular mechanism of the KIIIA interaction with hNav1.7, we utilized computational modeling and functional validation approaches as described below. The cryo-EM structure of the electric eel Nav1.4 (eeNav1.4) (19) channel was the closest structural homolog available to build the homology model of hNav1.7 when this study was conducted. The eeNav1.4 structure shares ~54% sequence identity with hNav1.7 overall and ~75% sequence identity over the hNav1.7 pore region. We used the RosettaCM modeling approach (20, 21) to generate a structural model of hNav1.7 based on the eeNav1.4 structure (19) and Rosetta protein-protein docking approach (21-23) to predict structure of KIIIA – hNav1.7 complex and specific residues forming interactions between KIIIA and hNav1.7 (see Methods). Our model revealed an asymmetrical binding of KIIIA to hNav1.7, where the KIIIA helical region is positioned perpendicular to the P2-helix in DII with the positively charged KIIIA residues facing the selectivity filter (Figure 1B). This orientation is different from KIIIA binding to the P2-helix in DIII previously suggested by computational modeling (15, 17) and lanthanide-based resonance energy transfer (24) studies. Mapping of the open space surrounding the KIIIA - hNav1.7 binding interface revealed a tunnel traversing from the extracellular environment to the channel pore cavity (Figure 1C). The minimum radius located at the most constricted part of tunnel within the selectivity filter region is of ~1 Å. Notably, the upper region of the selectivity filter near the KIIIA binding site has a minimum radius of ~2.5 Å, which is large enough to potentially allow sodium ion conduction and consistent with the characteristic incomplete block of Nav channels by KIIIA (13, 15). Notably, KIIIA is positioned just above the selectivity filter which is different from small molecular toxins, such as TTX and STX, which are positioned deeper into the selectivity region (25, 26).

Pairwise interactions identified from the KIIIA - hNav1.7 complex model

We examined contribution of the KIIIA residues to binding energy ($\Delta\Delta G$) in our KIIIA – hNav1.7 complex model (Figure 1D and E). $\Delta\Delta G$ was computed by taking the difference of the Rosetta energies of the KIIIA – hNav1.7 complex and the separated KIIIA and hNav1.7 structures. Our analysis revealed that the KIIIA residues K7, W8, R10, H12, and R14 each have significant contribution to the binding energy (Figure 1D and E). Notably, while K7, W8, R10, and H12 are located on the same face of KIIIA alpha helix, R14 is located within the C-terminal tail region. Our KIIIA – hNav1.7 model predicts that positively charged residue K7 forms a salt bridge with E919 on the P2-helix in DII (Figure 1F). In addition, W8 and H12 were shown to form hydrogen bonds with Y339 on the extracellular loop between S5 and P1-helix (S5P1) in DI and D923 on P2-helix in DII, respectively (Figure 1F). D11 is positioned near the interface between the P2-helices in DII and DIII and forms hydrogen bonds with both K7 on KIIIA and T1398 on the DIII P2 helix

(Figure 1F). The other positively charged KIIIA residues, R14 and R10, interact with two negatively charged residues: E1417 on the extracellular loop between the P2-helix and S6 (P2S6) in DIII and D1662 on the extracellular loop S5P1 in DIV. Notably, R14 also interacts with Y1416 on the extracellular P2S6 loop in DIII and contributes to a cation-pi interaction tower formed by Y1402 on the P2-helix in DIII, R896 on the extracellular loop S5P1 in DII, and Y1416. This position of R14 is different from the previously proposed proximity between R14 and D1241 on the P2-helix in DIII of rNav1.4 (15). However, the R10 position in proximity to I1399 on P2-helix in DIII is in agreement with the significant coupling energy between R10 and D1241 on P2-helix in DIII previously reported in rNav1.4 (15). We also observed the interaction between KIIIA N3 and E307 in the extracellular loop S5P1 in DI but this interaction may not be substantial as it is fully exposed in the bulk solvent. Indeed, N3 has been shown to be not critical for KIIIA interaction with rNav1.2 and rNav1.4 (13).

Functional mapping of KIIIA residues at toxin – channel interface

To characterize accuracy of our KIIIA – hNav1.7 model, we first tested the activity of the wild-type KIIIA on hNav1.7 using whole-cell voltage-clamp recordings as described in Methods. At the highest KIIIA concentration (10 μM) tested we observed up to ~90% inhibition of sodium current (Figure 2A), in agreement with previous studies (13, 15). To estimate the KIIIA binding affinity, we performed concentration-response experiments and obtained an IC_{50} of 0.40±0.08μM and 95% maximal block (Figure 2B,C), which is 4-fold higher than the K_d of 97 nM previously reported for hNav1.7 (15). In our tests, the wild-type KIIIA showed very slow dissociation from the wild-type hNav1.7 during the time-course of the whole-cell voltage-clamp experiments (Figure 2A, Table 1) compared to the previously published k_{off} of 0.017 min^{-1} suggesting that our Hill fit might be underestimating the affinity of the toxin. The extremely slow dissociation of WT-KIIIA from hNav1.7 complicated accurate determination of dissociation kinetics, as less than 10% recovery was observed during the time-course of experiments lasting up to ~30 min. Constraining single exponential fits of the dissociation data to assume maximum recovery, we obtained k_{off} between 0.002 min^{-1} and 0.005 min^{-1}. Extrapolation of the linear rate of recovery from these experiments provides an upper bound on the k_{off} of 0.003 min^{-1} and a K_d of 59 nM, respectively. We suggest that temperature differences between our experiments (~21ºC) and previously published experiments (~25ºC) might be responsible for the slower kinetics given the KIIIA binding site surrounded by the extracellular loop regions. Estimates of dissociation kinetics from constrained fits produce 7-fold higher affinity of ~59 nM, which is closer to the previously reported K_d of 97 nM (15) and likely underestimates KIIIA block at low toxin concentrations during our concentration-response experiment. Overall, the activity of WT-KIIIA on hNav1.7 in our experiments was similar to previously reported data (15).

We next performed an alanine scan of KIIIA residues that are positioned at the interface with hNav1.7 in our model. KIIIA substitutions K7A and H12A had nearly 100-fold decreases in affinity for the wild-type hNav1.7 channel in agreement with previously published data (13, 15, 16), likewise only K7A had a major effect on block, with reduction of maximal block by 20% (Figure 2C). Our data revealed that KIIIA substitutions W8A and D11A had a 50- and 10-fold reduction in affinity for the wild-type hNav1.7 channel, respectively (Figure 2D). Notably, these KIIIA mutations have not been previously tested against hNav1.7. For most KIIIA point mutations, the association rate remained similar to wild-type KIIIA, with only D11A showing a modest 3-fold increase in association rate (Figure 2D). The change in affinity was largely driven by between 36- and 116-fold increases in toxin dissociation from neutralizing mutations for the basic KIIIA

residues tested (Figure 2D). Kinetic data for k_{on}, k_{off}, K_d, and calculated fractional block at saturating concentration (F_{block}) are summarized in Table 1. KIIIA D11A substitution resulted in both an increase in k_{on} and k_{off}, which is potentially a result of the net increase in total charge caused by the mutation and the removal of a contact with T1398 on P2-helix in DIII according to our model. Notably, D11A substitution had no effect on dissociation from rNav1.2, but had a small effect on rNav1.4 binding—increasing k_{off} 4-fold, but with very little effect on k_{on} (13).

Table 1

Kinetics of toxin variants binding to WT-hNav1.7 from whole-cell voltage-clamp. experiments

Fractional block at saturating concentrations determined from extrapolation from kinetic data.

Channel and Toxin	k_{on} ($\mu M^{-1}min^{-1}$)	*SEM*	k_{off} (min^{-1})	*SEM*	K_d (μM)	*SEM*	*Fblock*	*SEM*
WT-hNav1.7 x WT-KIIIA	0.054	0.011	0.003	0.001	0.059	0.007	0.95[a]	0.033
WT-hNav1.7 x KIIIA-K7A	0.064	0.018	0.274	0.012	4.291	1.507	0.74	0.049
WT-hNav1.7 x KIIIA-W8A	0.110	0.045	0.329	0.097	2.990	1.719	0.90	0.094
WT-hNav1.7 x KIIIA-D11A	0.164	0.014	0.109	0.008	0.663	0.056	1.00	0.012
WT-hNav1.7 x KIIIA-H12A[b]	0.047	0.027	0.349	0.240	7.405	2.801	*0.88*	-

a – Fractional block was determined from the Hill fit of concentration-response data (fig 1c).

b – Fractional block reported by McArthur, et al., 2011(15) was used to constrain kinetic parameter estimates from association experiments.

Functional mapping of hNav1.7 residues at toxin – channel interface

To identify the key residues forming the KIIIA receptor site on hNav1.7, we selected mutations in the P2-helices in DI and DII in the outer pore based on our earlier KIIIA – hNav1.7 model based on the bacterial channel NavAb (PDB: 3RVY, (27, 28)), which was then superseded by our current KIIIA – hNav1.7 model based on eeNav1.4 structure shown in Figure 1. Notably, our earlier and current KIIIA – hNav1.7 models have the same hNav1.7 residues in the P2-helices in DI and DII interacting with KIIIA. We tested the N365 and Y362 residues on the P2-helix in DI and E919 and D923 on the P2-helix in DII. We selected these residues to inform the accuracy of the novel orientation of KIIIA in our model (Figure 1F). The E919A mutation did not produce measurable current. The E919Q mutation produced functional currents and reduced binding of the wild-type KIIIA by 42-fold (Figure 2E). The D923A mutation reduced affinity of the wild-type KIIIA by 40-fold (Figure 2E). N365A slightly increased toxin association, but made the block by KIIIA irreversible (Table 2). Y362C produced a modest increase in both association and dissociation yielding a 7.5-fold reduction in affinity (Figure 2E). This residue is of particular importance in TTX binding (29) and appeared to reduce the predicted maximal block by the wild-type KIIIA by ~20% (Figure 2C). Overall, hNav1.7 mutations E919Q, D923A, and Y362C reduce the binding of the wild-type KIIIA to hNav1.7 in agreement with our structural model of KIIIA – hNav1.7 complex and recent KIIIA – hNav1.2 structure (18).

Table 2

Kinetics of binding site mutations affecting WT-KIIIA from whole-cell voltage-clamp experiments

Fractional block at saturating concentrations determined from extrapolation from kinetic data.

Channel and Toxin	k_{on} ($\mu M^{-1}min^{-1}$)	*SEM*	k_{off} (min^{-1})	*SEM*	K_d (μM)	*SEM*	*Fblock*	*SEM*
WT-hNav1.7 x WT-KIIIA	0.054	0.011	0.003	0.001	0.059	0.007	0.95[a]	0.033
Y362C x WT-KIIIA	0.101	0.016	0.044	0.004	0.436	0.052	0.75	0.055
N356A x WT-KIIIA	0.086	0.006	irreversible	-	n.d.	-	n.d.	-
E919Q x WT-KIIIA	0.040	0.003	0.101	0.003	2.51	0.16	0.92	0.028
D923A x WT-KIIIA	0.083	0.022	0.193	0.022	2.34	0.41	0.89	0.037

a – Fractional block was determined from the Hill fit of concentration-response data (fig 1c)

Double Mutant Cycle Analysis of Key pairwise interactions between KIIIA and hNav1.7

To validate our KIIIA – hNav1.7 model using double mutant cycle analysis (30), we performed double-mutant experiments isolating the contributions of specific pairwise contacts to the binding energy between KIIIA and hNav1.7 (Figure 3). With KIIIA substitutions at positions K7, D11, and H12, and hNav1.7 mutations E919Q, D923A we were able to compare the single mutant to double-mutant effects to evaluate thermodynamic cycles (Figure 3A). Pairwise contacts can be identified on the basis of the path-independence from the wild-type condition to the double-mutant condition: the reduction in binding energy resulting from a mutation to either side of an interacting pair should be non-additive in the double-mutant condition (30). Residue pairs that exhibit additive effects of the double-mutant relative to the single mutants would be expected to make little functional interaction. These effects are quantified by calculating the coupling coefficient and the coupling energy (see Methods). Strongly interacting residue pairs will have coupling coefficients significantly different from 1.0, while non-interacting pairs will trend towards a coupling coefficient close to 1 (30). While an apparent coupling of residues determined by this method can result from allosteric effects, combination with computational modeling and structural studies may suggest a direct interaction. We tested the following pairs of double mutants: E919Q x K7A, D923A x H12A, which both directly interacted in our model (Figure 4A), and E919Q x D11A, which did not interact directly in our model. E919Q x D11A greatly reduced the toxin affinity (K_d =14.2±5.8 μM) relative to either of the single mutations, E919Q and D11A (2.34±0.16 μM and 0.66±0.06 μM, respectively) (Figure 3B and Table 3), with a coupling coefficient of 0.5 and a coupling energy of 0.4 kcal·mol $^{-1}$ (Table 4). For E919Q and K7A the double-mutant showed similar binding affinity (2.47±1.32 μM to the channel mutation alone (2.51±0.16 μM), while both had a lower affinity than the K7A variant on the wild-type channel (4.29±1.51 μM) (Figure 3A and Table 3). The D923A mutation reduced the affinity of KIIIA and did not have an additive effect with H12A (Figure 3A and Table 3). We calculated the coupling coefficients and coupling energies for the pairs as described in the materials and methods. We found strong coupling energies between H12 on KIIIA and D923 on hNav1.7 (2.8 kcal·mol^{-1}) (Table 4). We also found strong coupling energies between K7 on KIIIA and E919 on hNav1.7 (2.5 kcal·mol^{-1}) (Table 4). These results are consistent with the interactions observed in our model (Figure 4A) and the recent structure of KIIIA - Nav1.2 complex (18).

Table 3

Kinetics of double-mutant cycle pairs from whole-cell voltage-clamp experiments.

Fractional block at saturating concentrations determined from extrapolation from kinetic data.

Channel and Toxin	k_{on} ($\mu M^{-1}min^{-1}$)	*SEM*	k_{off} (min^{-1})	*SEM*	K_d (μM)	*SEM*	*Fblock*	*SEM*
WT-hNav1.7 x WT-KIIIA	0.054	0.011	0.003	0.001	0.059	0.007	0.95[a]	0.033
WT-hNav1.7 x KIIIA-K7A	0.064	0.018	0.274	0.012	4.29	1.51	*0.74*	0.049
WT-hNav1.7 x KIIIA-D11A	0.164	0.014	0.109	0.008	0.66	0.056	*1.00*	0.012
WT-hNav1.7 x KIIIA-H12A[b]	0.047	0.027	0.349	0.240	7.40	2.80	*0.88*	-
E919Q x WT-KIIIA	0.040	0.003	0.101	0.003	2.506	0.16	0.92	0.028
E919Q x KIIIA-K7A	0.044	0.015	0.108	0.021	2.466	1.32	0.48	0.066
E919Q x KIIIA-D11A	0.124	0.046	4.640	0.461	14.19	5.79	0.92	0.028
D923A x WT-KIIIA	0.083	0.022	0.193	0.022	2.34	0.41	0.89	0.037
D923A x KIIIA-H12A	0.183	0.065	0.440	0.098	2.40	1.45	0.49	0.092

a – Fractional block was determined from the Hill fit of concentration-response data (fig 1c).

b – Fractional block reported by McArthur, et al., 2011(15) was used to constrain kinetic parameter estimates from association experiments.

Table 4

Coupling coefficients and coupling energies from double-mutant cycle experiments

	D923A x H12A	*E919Q x K7A*	*E919Q x D11A*
$E_{coupling}$ $kcal \cdot mol^{-1}$	*2.81*	*2.51*	*0.40*
Ω	*0.008*	*0.014*	*0.50*

Marked difference for KIIIA binding specificity among Nav channel isoforms

The differences in KIIIA binding affinity between the Nav channel isoforms likely arises from multiple sequence difference within the toxin binding site (Figure 4A and B). The recent structure of the KIIIA - hNav1.2 complex (31) confirmed the predictions from our structural model of the KIIIA - hNav1.7 complex with high accuracy. The backbone root mean square deviation (RMSD) of the KIIIA - hNav1.7 model and the KIIIA - hNav1.2 structure over the toxin binding region (formed by KIIIA, P1-helix, P2-helix, and extracellular loops) is ~1.0 Å. Specific pairwise contacts between K7-E919 and H12-D923 in our KIIIA - hNav1.7 model validated by mutant cycle analysis appeared to be exact in the KIIIA - hNav1.2 complex structure with the corresponding pairwise contacts between K7-E945 and H12-D949 (Figure 4A and B) (31). Our KIIIA - hNav1.7 model also correctly predicted other non-tested contacts, including pairwise interactions between KIIIA N3 and W8 with E307 and Y339, respectively, on the extracellular S5-P1 loop of DI (Figure 4A and B). On the DI P2 helix, Y362 and N365 potentially contribute to the difference in specificity between the TTX-sensitive and TTX-nonsensitive isoforms. In the TTX-

nonsensitive channels hNav1.5, hNav1.8, and hNav1.9, the corresponding residues are either Cys or Ser (for Y362) and Arg (for N365) (Figure 4B). Having a non-aromatic residue at Y362 position and Arg at the N365 position could severely influence interaction with K7 on KIIIA.

Interestingly, the KIIIA residues D11 and R10 in our KIIIA - hNav1.7 model are positioned similarly in the KIIIA - hNav1.2 structure, but details of toxin – channel interactions are different (Figure 4A). D11 forms a hydrogen bond with T1398 on the P2-helix in DIII in our KIIIA - hNav1.7 model (Figure 4A), but the substitution of Thr (T1398) hNav1.7 to Met (M1425) on the P2-helix in DIII in hNav1.2 removes this potential interaction and promoting a new hydrogen bond to be formed with the nearby residue Y1429 (31). Remarkably, residues T1398 and I1399 on the P2-helix in DIII of hNav1.7 are Met and Asp, respectively, in all other human Nav channels. R10 interacts with D1426 on the DII P2-helix in the hNav1.2 structure but the corresponding position in hNav1.7 is I1399 (Figure 4A and B). This difference potentially contributes to R10 interaction with the nearby acidic residue D1662 on the DIV extracellular S5-P1 loop in hNav1.7. Notably, Asp at position 1662 is only present in hNav1.7 - corresponding residues at this position in other Nav channel subtypes are Val, Ala, and Ser (Figure 4B).

We also identified several additional positions on the extracellular loop regions of Nav channels that may contribute to specific interactions between KIIIA and Nav channels. Both our KIIIA - hNav1.7 model and the KIIIA - hNav1.2 structure show the positively charged R14 forming cation – π interactions with Y1416 (hNav1.7) or Y1443 (hNav1.2) on the extracellular P2-S6 loop in DIII. Notably, in the KIIIA - hNav1.2 structure R14 is also in proximity to the negatively charged E919 on the extracellular S5-P1 loop in DII (31). However, in our KIIIA - hNav1.7 model R14 is in proximity to T893 on the extracellular S5-P1 loop in DII (which is corresponding to E919 in hNav1.2) and E1417 on the extracellular P2-S6 loop in DIII (Figure 4A and B). These structural and sequence differences might be responsible for KIIIA R14A mutant selectivity for hNav1.7 versus hNav1.2 (15).

Difference in structural dynamics of KIIIA binding to hNav1.7 and hNav1.2 revealed by molecular dynamics simulations

To further study the molecular mechanism of the KIIIA interaction with hNav1.7, we performed molecular dynamics (MD) simulation of our KIIIA - hNav1.7 complex model, as described in Methods. The 1μs simulation revealed relatively stable binding of KIIIA within the receptor site with notable dynamics of specific KIIIA residues. During the simulation the RMSD of hNav1.7 pore residues reached ~5Å and at the interface between KIIIA and hNav1.7 was ~4Å (Figure 5A). At the beginning of the simulation, a sodium ion is binding to E919 and E916 on the P1-P2-helix region in DII (Figure 5A). This agrees with the density identified as a sodium ion at the same position in the cryo-EM structure of the hNav1.2-KIIIA complex. Our MD simulation revealed that this sodium ion quickly diffused out to the extracellular bulk via the open passage formed between the KIIIA and channel, supporting the incomplete channel block observed in experiments (Figure 2) (13, 15). After the escape of the sodium ion from the selectivity filter, the KIIIA - hNav1.7 structure relaxed in this state for about 100 ns and then dynamically changed towards a slightly different binding state in which K7 on KIIIA formed interactions with Y362 and E364 on the P2-helix in DI, and D1690 on P2-helix in DIV (Figure 5A). This agrees with our functional characterization of KIIIA - hNav1.7 interactions where we observed a 100-fold reduction in K_d for the K7A mutation on KIIIA and only a 42-fold reduction for E919Q mutation on the channel, a

mutation that may not completely disrupt interaction at the 919 site with K7. R10 is still neighboring I1399 on the P2-helix in DIII and switched from interacting with D1662 on the extracellular S5-P1 loop in DIV to interacting with D1690 on the P2-helix in DIV (Figure 5A). Interestingly, with both K7 and R10 reaching towards the P2-helix in DIV during the MD simulation, the channel appeared to be more completely blocked in this configuration. In addition, we also observed dynamic coupling of other key residues on KIIIA with P2-helices and extracellular loop regions of hNav1.7 (Figure 5A). W8 interacted with K310 and Y339 on the extracellular S5-P1 loop in DI. H12 showed significant interactions with D923 on the P2-helix in DII and also with the backbone of P895 on the extracellular S5-P1 loop in DII. D11 is positioned deep at the interface between DII and DIII formed by W897 on the extracellular S5-P1 loop and E919 in P2-helix in DII and T1398 and Y1402 on P2-helix in DIII. R14 primarily interacted with Y1416 on the extracellular P2-S6 loop in DIII and did not maintain interaction with E1417 on the extracellular loop in DIII as identified in our model. Notably, R14 also formed interactions with T893, L894, and P895 on the extracellular S5-P1 loop in DII (Figure 5A).

We also studied the structural dynamics of the KIIIA interaction with hNav1.2 using the recently published cryo-EM structure of the KIIIA - hNav1.2 complex. Our MD simulation revealed relatively stable binding of KIIIA within the receptor site with notable dynamics of specific KIIIA residues. During the simulation the RMSD of the hNav1.2 pore residues reached ~5Å and at the interface between KIIIA and hNav1.2 was ~4Å (Figure 5B). The sodium ion in the selectivity filter at the site formed by E942 and E945 on the P1-P2-helix region in DII of hNav1.2 quickly diffused out to the extracellular bulk, again in agreement with an incomplete block of KIIIA on Nav1.2 (13) and our simulation of the KIIIA - hNav1.7 model (Figure 5A and B). In contrast to our KIIIA – hNav1.7 simulation, after the escape of the sodium ion, we did not observe the transition of K7 to form interactions with E387 on P2-helix in DI and D1717 on P2 helix in DIV. K7 formed more stable interactions with E945 on the P2-helix in DII, and also N361, Y362 on the extracellular S5-P1 loop in DI. In contrast to the KIIIA - hNav1.7 simulation, R10 stably interacted with D1426 on P2-helix in DIII (Figure 5B) and did not form new interactions with D1717 on P2-helix in DIV. This configuration of K7 and R10 promoted a slight rotation of the KIIIA helical region around the principal axis and allowed other key residues to make new interactions with hNav1.2. Aside from Y362, W8 also interacted with other residues in the DI loop including N361 and K333. Interestingly, H12 mainly interacted with Y362 on the extracellular S5-P1 loop in DI and I914 and S915 on S5-P1 loop in DII (Figure 5B). D11 slightly shifted towards the P2-helix in DII and interacted with Y362 on the extracellular S5-P1 loop in DI and E945 on the P2-helix in DII. Similar to the KIIIA - hNav1.7 simulation, R14 stably interacted with Y1443 on the extracellular P2-S6 loop in DIII and E919 and L920 on the extracellular S5P1 loop in DII (Figure 5B).

We found intriguing specific differences in the K7 dynamics between KIIIA – hNav1.7 and KIIIA – hNav1.2 MD simulations. Notably, D1426 on P2-helix in DIII of hNav1.2 is conserved among all other Nav channel isoforms, except for hNav1.7, which has I1399 at this position (Figure 4). The absence of Asp at the 1399 position in hNav1.7 allowed the transition of R10 to interact with the nearby acidic residue D1690 on the P2-helix in DIV, and also promoted interaction of K7 with E364 on the P2-helix in DI and D1690 to have a more complete block of the channel as observed in the hNav1.7-KIIIA simulations. Indeed, the functional studies showed that the mutation of Asp to Ile in Nav1.4 (D1241) at position corresponding to I1399 in hNav1.7 increased the fractional

block, while the reversed substitution of Ile to Asp in Nav1.7 decreased the fractional block (15). In addition, R10A produced a 35% reduction in KIIIA block of Nav1.4, while the loss of toxin block caused by the R10A mutation was largely rescued by the Nav1.7-like Ile in the DIII P2 helix (15). These results suggest that the differential interactions that we observed here between KIIIA and hNav1.7 and hNav1.2 may indicate a potential structural basis for differences in molecular determinants of KIIIA binding to hNav1.7 versus other Nav channel isoforms.

Discussion

The cryo-EM structure of the KIIIA - hNav1.2 complex was published in January of 2019 (18) while this manuscript was in preparation. Our computational model of hNav1.7, docking of KIIIA to the hNav1.7 model, and functional testing of KIIIA and hNav1.7 mutations presented here were completed prior to the publication of KIIIA - hNav1.2 complex structure and the availability of the PDB coordinates. While hNav1.7 and hNav1.2 channels share sequence homology within most of the KIIIA binding region, they exhibit several key differences at the toxin - channel interface. Our computational structural modeling and experimental validation revealed that our KIIIA - hNav1.7 model agrees with the hNav1.2-KIIIA complex structure. Strikingly, we accurately predicted and functionally characterized specific pairwise contacts between K7 on KIIIA and E919 on the P2-helix in DII and also H12 on KIIIA and D923 on the P2-helix in DII. The similarity between our KIIIA – hNav1.7 model and the KIIIA – hNav1.2 structure highlights the predictive power of our structural modeling and functional testing approach with potential future applications to study other peptide toxin – channel interactions.

Our MD simulations provide comprehensive understanding of the dynamics of KIIIA binding to hNav1.7 and hNav1.2 channels that are beyond the static hNav1.7-KIIIA model and the hNav1.2-KIIIA structure. Different stable configurations of KIIIA binding to hNav1.7 and hNav1.2 revealed the importance of the P2-helix in DIII binding site where I1399 is potentially responsible for creating a more complete block in hNav1.7. Due to the dynamic nature of KIIIA binding to Nav channels as revealed by our simulation, we cannot rule out that both binding configurations may happen in hNav1.7 and hNav1.2 channels but with different fractions of time.

Another feature of the molecular mechanism of KIIIA binding are differences in the reversibility and irreversibility of some of the KIIIA mutants on different Nav channels. Cryo-EM structures of hNav1.2, hNav1.4, and hNav1.7 channels (25, 31, 32) revealed that the extracellular vestibule of the channel pore targeted by KIIIA is surrounded by several relatively long loop regions raising the possibility that KIIIA access pathway to the toxin binding site is relatively narrow. Restricted access and escape pathways for KIIIA binding agree with the relatively slow k_{on} and k_{off} rates observed in previously published data (2, 13, 15) and our functional studies (Figures 2 and 3).

Our computational modeling and functional testing approach to study molecular determinants of toxin – channel interactions can be potentially expanded to rational design of small peptides to target the selectivity region of Nav channels using Rosetta protein design approaches (33-35). The sequence differences between Nav channels in the pore extracellular loop regions and P2-helices suggest that protein design and optimization could create inhibitors selective for any Nav channel subtype. Novel, high-affinity, selective inhibitors of Nav channels will have transformative potential to define a new class of biologics to treat Nav channel related diseases, such as, chronic pain, cardiac arrhythmias, and epilepsy.

Conclusions

We generated a structural model of the KIIIA in complex with hNav1.7 and validated it by functional testing using alanine-scan mutagenesis of KIIIA and hNav1.7 and double mutant cycle analysis of specific pairwise toxin – channel interactions. Our structural model was further validated by long time-scale unbiased MD simulations of the KIIIA - hNav1.7 complex, which confirmed that acidic residues E919 and D923 on the P2-helix in DII of Nav1.7 contribute significantly to the binding energy, and that KIIIA forms multiple interactions with the extracellular loops in DI-III. Overall, our results are consistent with previously published experimental studies and reveal molecular determinants of the KIIIA interaction with human Nav channels. Our approach can be potentially useful for engineering of molecular probes to study Nav channels function and for rational design of novel therapeutics to treat chronic pain, cardiac arrhythmias, and epilepsy.

Acknowledgements

We would like to thank Drs. Heike Wulff, Jie Zheng, and Igor Vorobyov, and members of Yarov-Yarovoy and Sack laboratories for helpful discussions. We thank Dr. Nieng Yan (Princeton University) for sharing coordinates of electric eel and human Nav1.2 channel structures, and independent comparison of our KIIIA – hNav1.7 model to coordinates of KIIIA – hNav1.2 structure prior to release in Protein Data Bank. We thank Dr. Christoph Lossin (University of California, Davis) for providing hNav1.7 cell line and channel constructs, as well as Dr. William Catterall (University of Washington) for the tsa201 cell line. Anton 2 computer time was provided by the Pittsburgh Supercomputing Center (PSC) through Grant R01GM116961 from the National Institutes of Health. The Anton 2 machine (36) at PSC was generously made available by D.E. Shaw Research. This research was supported by National Heart, Lung, and Blood Institute Grants U01HL126273 and R01HL128537 to VYY, UC Davis Academic Senate Award FL18YAR to VYY, NIH T32 GM099608 to IHK, and AHA 17PRE33670204 to IHK.

Materials and Methods

Homology modeling of hNav1.7 based on EeNav1.4 structure

The cryo-EM structure of the Nav1.4-beta1 complex from the electric eel (eeNav1.4) (PDB ID: 5XSY) (19) was used to generate the model of hNav1.7 channel using Rosetta structural modeling software (20, 21). Initially, we refined the published coordinates of eeNav1.4, without the beta1 subunit by using the Rosetta cryo-EM refinement protocol (37) and picked the lowest scoring density-refitted eeNav1.4 model to use as a template. The comparative modeling protocol RosettaCM (20) was then used in combination with the electron density of the eeNav1.4 to model the hNav1.7 structure. We generated 5,000 structural models of hNav1.7 and selected the top 500 lowest-scoring models for clustering analysis as described previously (38). Visual inspection of the top scoring clustered models was used to select the final model for the docking study.

Molecular docking of KIIIA to the hNav1.7 model

The solution NMR structure of KIIIA (PDB ID: 2LXG) (14) was used as an ensemble to dock to the hNav1.7 model using the RosettaScript XML scheme (21, 39). At first, we found that it is challenging for Rosetta to move the KIIIA structures to pass the narrow passage created by the extracellular loops to fully sample the binding site. We divided the docking protocol into two subsequent stages. In stage 1, docking was performed with the DI S5P1 and DIII S5P1 loops truncated and using full random translational and rotational perturbation of KIIIA at both low and high-resolution phases. This stage generated 20,000 structural models of the docking complexes. We then selected the top 1,000 models based on the total scores and filtered based on the Rosetta $\Delta\Delta$G (an estimate of the binding energy of a complex) to select the top 500 models. $\Delta\Delta$G was computed by taking the difference of the Rosetta energies of the KIIIA – hNav1.7 complex and the separated KIIIA and hNav1.7 structures. We clustered these complexes using the Rosetta legacy clustering application. The center models of top 20 clusters then passed to stage 2 docking. In this stage, positions of KIIIA in the top 20 clusters were used to create 20 different starting docking trajectories with the full structure of hNav1.7 model including all the extracellular loop regions. The full translational and rotational perturbation used in the previous stage was turn off. Instead, only limited local perturbation was allowed in both centroid and full-atom refinement phases. Similar to stage 1, we generated 20,000 structural docking models and filtered based on the Rosetta total score and $\Delta\Delta$G to select top 500 models, which then were clustered to finalize top 5 complexes for visual inspection. The selected docking model presented here has the best Rosetta $\Delta\Delta$G and is the only one in the top 5 clusters models show good agreement with previously published data.

Molecular dynamics simulation of hNav1.7-KIIIA and hNav1.2-KIIIA complexes

The docking complex of hNav1.7-KIIIA and the cryo-EM structure of hNav1.2 (PDB ID: 6j8e) were used to setup systems for MD simulations. For the hNav1.2 structure, Rosetta density refinement protocol was applied as described above for the hNav1.7. The missing region on DI extracellular loop was modeled using Rosetta loop modeling. CHARMM-GUI (40) was used to embed the hNav1.7-KIIIA model and the hNav1.2-KIIIA structure (PDB ID: 6j8e) in a lipid

bilayer of POPC with explicit TIP3P water molecules at a concentration of 150 mM NaCl. CHARMM36 forcefield was used for proteins, lipids, and waters in both systems. Equilibrations were run on our local GPU cluster using NAMD version 2.12 (41). After 10,000 steps of steepest descent minimization, MD simulations started with a timestep of 1 fs with harmonic restraints initially applied to protein heavy atoms and some lipid tail dihedral angles as suggested by CHARMM-GUI (40). These restraints were slowly released over 2 ns. Harmonic restraints (0.1 kcal/mol/Å2) were then applied only to protein backbone atoms, and the systems were equilibrated further for 20 ns with a timestep of 2 fs. All bonds to H atoms were constrained using the SHAKE algorithm in order to use a 2 fs timestep. Simulations were performed in NPT ensemble with semi-isotropic pressure coupling to maintain the correct area per lipid, and constant temperature of 303.15 K. Particle Mesh Ewald (PME) method was used to compute electrostatic interactions. Non-bonded pair lists were updated every 10 steps with a list cutoff distance of 16 Å and a real space cutoff of 12 Å with energy switching starting at 10 Å.

We used the Anton 2 software version 1.31.0 for production runs of 1us of each system on the Anton 2 supercomputer. Simulations were performed in the NPT ensemble at 303.15 K A with 2 fs timestep. Non-bonded long-range interactions computed every 6 fs using the RESPA multiple time step algorithm. The multi-integrator algorithm was used for temperature and semi-isotropic pressure coupling and the u-series algorithm was used for long-range electrostatic interactions. A long-range Lennard-Jones (LJ) correction (beyond cutoff) was not used as was suggested for CHARMM36 lipid force field.

Cell culture and preparation

Electrophysiology experiments were performed on transiently transfected tsa-201 cells (gift from William Catterall) and a HEK 293T cell line stably expressing hNav1.7 (gift from Chris Lossin). Cells were grown at 37ºC, 5% CO_2 in DMEM with high glucose, L-glutamine, and Sodium Pyruvate (Gibco) with 10% FBS, and 1% Penicillin/Streptomycin. The stable cell line was raised in the same conditions with G418 as a selection agent. Cells were grown to 70% confluency in 35mm dishes and passaged every 2-3 days for tsa-201 and 3-4 days for the stable-cell line. Cells were washed with DPBS (Gibco) and dissociated with 0.05% Trypsin-EDTA (Gibco) and seeded to fresh dishes with pre-warmed media. tsa-201 cells were transfected via Lipofectamine 2000 24-48 hours prior to experiments with 1 μg pCMV6-hNav1.7(and mutants) and 0.5 μg pMaxGFP for identification of transfected cells. Prior to experiments cells were washed with DPBS and dissociated in Versene (Gibco) and scraped from the dishes and transferred to a 14mL conical tube in 3:1 DMEM:Versene. They were centrifuged at 1000 x *g* for 2 minutes and resuspended in a microfuge tube in 1mL extracellular solution with 10 mM D-glucose and rotated at RT until use.

Toxin preparation

Lyophilized WT-KIIIA was purchased (Alomone labs, Jerusalem, IS), reconstituted in water and stored as 100 μM stock aliquots at -80ºC prior to use. Toxin variants were produced by solid state synthesis as described previously (13) and stored as stock aliquots at -80ºC prior to use. Stock concentrations were checked by Nanodrop with extinction coefficients determined by the ExPASy ProtParam online tool (42). Stock aliquots of toxin were suspended in 2xExternal solution with

0.2% BSA for working solutions of toxin in vehicle of 1xExternal solution with 0.1% BSA. Vehicle for controls were prepared in the same manner.

Electrophysiology

Whole-cell voltage-clamp recordings were performed at RT (~21-22ºC) in a 100 μL recording chamber mounted on a Zeiss Axiovert 35 microscope illuminated with a Zeiss HBO 100W AttoArc lamp and filter set for epifluorescent detection of GFP expressing cells. Approximately 40 μL of cell suspension was added to the pre-filled chamber and allowed to adhere to the glass bottomed chamber for 2-10 minutes. Fresh external solution was perfused through the chamber prior to patching. 1-2 MΩ borosilicate pipettes (Sutter instruments) pulled, fire-polished, coated with Sylgard, and filled with the internal recording solution. GFP expressing cells were patched and signals were amplified with an Axon Axopatch 200-B (Molecular Devices). GΩ seals were obtained, and pipette capacitance was corrected for prior to break-in achieved by suction. Access resistance (R_s) was typically 1-4 MΩ. 60%-80% R_s compensation was used to reduce voltage error to less than 10mV. P/5 leak subtraction protocol was used during recording. Signals were filtered with a low-pass Bessel filter at 5-10 kHz. Signals were digitized at [20 kHz? check] and recorded with Patchmaster (version)(HEKA) on a Windows 7 PC. The solutions were as follows in mM: External 3.5 KCl, 155 NaCl, 10 HEPES, 1 $MgCl_2$, 1.5 $CaCl_2$ adjusted to pH 7.4 with NaOH, and 315 mOsm; Internal: 35 NaCl, 70 CsCl, 50 CsF, 1 EGTA, 10 HEPES adjusted to pH 7.4 with CsOH at 310 mOsm. After break-in, cells were held at -120 mV and tested for stable Na^+ current with depolarizing 35 ms voltage steps to -10 mV from -120 mV collected every 5 s for up to 5 minutes to allow for a stable level of current prior to vehicle addition. Once stable current levels were achieved, 150 μL of vehicle was added to the bath via pipette with displaced solution removed via an overflow vacuum line. After approximately? pulses (minutes?) whole cell parameters were checked, and toxin was added via pipette as with vehicle during recording, with vacuum suction removing displaced bath solution. Once apparent block plateaued, whole cell parameters were re-checked, and pulsing resumed. To measure dissociation, gravity fed perfusion with fresh external solution was started at a rate 1-2 mL/min during recording.

Data analysis

Electrophysiology data were analyzed and plotted in IGOR 7 Pro (Wavemetrics). Geometric means of kinetic parameters were determined using Excel (Microsoft) and plotted in IGOR 7 Pro. Peak currents during depolarizations were plotted by time and data were fit with single exponential function (equation 2) during association and dissociation to get tau values shown. The association rate k_{on} was determined by equation 3, k_{off} was determined by equation 4. Affinity was determined kinetically as the dissociation constant K_d via equation 5. The slow dissociation of WT-KIIIA from WT-hNav1.7 made thorough measurement of k_{off} difficult, thus values shown here are best estimates from fits with the amplitude constrained based on the maximal current before toxin association. The resulting values of affinity are consistent with previous reporting of kinetic determination of affinity for this channel (15). IC_{50} was determined for WT-KIIIA x WT-hNav1.7 to estimate the maximal block (equation 1). The IC_{50} was higher than expected, though when used place of K_d for coupling energy calculations the coupling energies for D923A x H12A and E919Q x K7A remain above our threshold of 1.0 kcal/mol. The low affinity of H12A hindered precise

measurement of kinetics, thus the rates are extrapolated from Fractional block assuming maximal block at saturating concentration of 0.877 as reported previously (15).

Equations:

[1] Hill equation to determine residual current: $I_{Na^+} = 1 - \frac{1}{1+\frac{[Tox]^h}{IC_{50}}}$

[2] Single exponential fit for association and dissociation kinetics: $I_{Na^+} = y_o + Ae^{-t-t_0/\tau}$

[3] Association rate: $k_{on} = \frac{\frac{1}{\tau_{on}} - k_{off}}{[tox]}$

[4] Dissociation rate: $k_{off} = \frac{1}{\tau_{off}}$

[5] Affinity: $K_d = \frac{k_{off}}{k_{on}}$

[6] Fractional block at saturating concentration: $F_b = F_{[tox]}\left(1 + \frac{K_d}{[tox]}\right)$

[7] Coupling Coefficient: $\Omega = \frac{K_d ww * K_d mm}{K_d wm * K_d mw}$

[8] Coupling Energy: $E_{coupling} = -RT \ln \Omega$

Figure Legends

Figure 1: Homology model of hNav1.7-KIIIA features asymmetric binding of toxin to the outer pore. (**A**) Structure and sequence of KIIIA (PDB: 2LXG) (14) shows alpha helical core stabilized by three disulfide bridges and with and amidated C-terminus. (**B**) Extracellular view of our homology model of KIIIA – hNav1.7 complex based on the EeNav1.4-β1 cryo-EM structure (19). Channel domains are depicted according to color keys, and KIIIA is depicted in pink with the ribbon and surface shown. KIIIA binds asymmetrically to the outer pore between DII and DIII. (**C**) Side view of channel pore and selectivity filter region with KIIIA bound (pink) and cavity volume colored by diameter shows that main constriction point is still the selectivity filter with enough room for Na^+ conduction. (**D**) Rosetta ΔΔG determination identified residues K7, W8, R10, H12, and R14 as significant contributors to binding energy. (**E**) Heatmap of Rosetta ΔΔG shows the importance of the helical region for binding. (**F**) Detailed view of interacting residues at KIIIA – hNav1.7 interface predicted by our model.

Figure 2: Functional mapping of KIIIA and hNav1.7 residues at toxin – channel interface. (**A**) WT-KIIIA blocks WT-hNav1.7 incompletely; I*t plot of peak I_{Na}+ data from a single experiment and example current traces colored from first to last (red to blue), purple dots represent values in I*t plot (inset). (**B**) Hill-fit of concentration-response data for WT-KIIIA against hNav1.7 in HEK293 cells (IC_{50}=0.40±0.08 μM mean±sd, n=2-4 cells per concentration), from maximum block recorded during association-dissociation experiments (right). (**C**) Calculated maximal block of KIIIA and its analogs from association-dissociation experiments. WT-hNav1.7 x H12A block data from McArthur, et al (15). (**D**) Kinetic data from electrophysiological measurements show general agreement with Rosetta predicted energies. Alanine variants of residues K7, W8, D11, and H12 showed significant reductions in affinity (left), little change in association (middle), but marked increases in toxin dissociation (right). Bars are geometric mean±sd from n=3-5 cells per variant, empty circles represent single cells. (**E**) Mutations to channel residues demonstrate reductions in affinity of the WT-KIIIA from Y362C, E919Q, and D923A (left), little change to toxin association (middle), and increases in dissociation (right), similar to the effects of toxin variants.

Figure 3: Double Mutant Cycle Analysis of key pairwise interactions between KIIIA and hNav1.7. (**A**) Double-mutant thermodynamic cycles between K7A x E919Q, H12A x D923A, and D11A x E919Q. values indicate difference from expected values if no interaction occurs. (**B**) Kinetic data for single and double mutants. The double mutants for K7A x E919Q and H12A x D923A were similar to the respective single mutant conditions, while the D11A x E919Q double mutant showed a much greater reduction in affinity relative to the single mutants (bars are geometric mean±sd, n=2-5 cells per condition, empty circles are individual cells).

Figure 4: Structural difference for KIIIA binding specificity among Nav channel isoforms. (**A**) Our hNav1.7 model closely resembles the hNav1.2-β2-KIIIA cryo-EM structure especially at the key interacting points on the DII-P2 helix (left). The key sequence difference in DIII between Nav1.7 and all other isoforms T1398 I1399 vs MD, eliminates a key interaction with R10 seen in the cryo-EM structure, and introduces an interaction between D11 and T1398 (middle). The proximity of R10 to the conduction pathway is of particular importance to toxin efficacy. (Right) R14 makes contacts with DIII residues in both the cryo-EM structure and our model, though slight

sequence differences and rotamers change the character of this interaction. T893 in DII is near R14, though is a glutamate in Nav1.2, and the E1417 in DIII adopts a different conformation to interact directly with R14 in our model while the two are separate in the Nav1.2 structure. (**B**) Sequence alignment of the different Nav subtypes with contact points (orange) and neighboring residues (yellow) show few sequence differences between the channel subtypes at the points of contact. The most prominent differences are in DIII T1398-I1399 and DIV D1609, which is an A, V, or S in all other subtypes, both of which sit near R10 in our model.

Figure 5: MD simulation of hNav1.7-KIIIA and hNav1.2-KIIIA complexes. (**A**) Structural dynamics of KIIIA binding in hNav1.7. Snapshots of KIIIA binding configurations with hNav1.7 during the simulation, associated with the interface RMSD (left and middle panels): 1, an equilibrated configuration with sodium ion in the selectivity filter; 2, a relaxed configuration after the escape of selectivity filter sodium ion; 3, stable configuration with K7, R10 reaching toward DIV P2 helix. Heatmap showing the probability of forming contacts between key residues on KIIIA and hNav1.7 channel during the simulation (right panel). (**B**) Structural dynamics of KIIIA binding in hNav1.2. Snapshots of KIIIA binding configurations with hNav1.2 during the simulation, associated with the interface RMSD (left and middle panels): 1, an equilibrated configuration with sodium ion in the selectivity filter; 2, a more stable configuration with strong interaction of R10 and D1426. Heatmap showing the probability of forming contacts between key residues on KIIIA and hNav1.2 channel during the simulation (right panel).

References

1. Hille B (2001) *Ion Channels of Excitable Membranes* (Sinauer Associates, Sunderland, MA)) 3rd Ed.
2. Wilson MJ, *et al.* (2011) mu-Conotoxins that differentially block sodium channels NaV1.1 through 1.8 identify those responsible for action potentials in sciatic nerve. *Proc Natl Acad Sci U S A* 108(25):10302-10307.
3. Catterall WA, Goldin AL, & Waxman SG (2005) International Union of Pharmacology. XLVII. Nomenclature and structure-function relationships of voltage-gated sodium channels. *Pharmacol Rev* 57(4):397-409.
4. Dib-Hajj SD, Cummins TR, Black JA, & Waxman SG (2010) Sodium channels in normal and pathological pain. *Annual review of neuroscience* 33:325-347.
5. Dib-Hajj SD, Yang Y, Black JA, & Waxman SG (2013) The Na(V)1.7 sodium channel: from molecule to man. *Nat Rev Neurosci* 14(1):49-62.
6. Lampert A, Eberhardt M, & Waxman SG (2014) Altered sodium channel gating as molecular basis for pain: contribution of activation, inactivation, and resurgent currents. *Handb Exp Pharmacol* 221:91-110.
7. Nguyen PT, DeMarco KR, Vorobyov I, Clancy CE, & Yarov-Yarovoy V (2019) Structural basis for antiarrhythmic drug interactions with the human cardiac sodium channel. *Proc Natl Acad Sci U S A* 116(8):2945-2954.
8. Yarov-Yarovoy V, *et al.* (2002) Role of amino acid residues in transmembrane segments IS6 and IIS6 of the Na+ channel alpha subunit in voltage-dependent gating and drug block. *J Biol Chem* 277(38):35393-35401.
9. Yarov-Yarovoy V, *et al.* (2001) Molecular determinants of voltage-dependent gating and binding of pore-blocking drugs in transmembrane segment IIIS6 of the Na(+) channel alpha subunit. *J Biol Chem* 276(1):20-27.
10. Ragsdale DS, McPhee JC, Scheuer T, & Catterall WA (1994) Molecular determinants of state-dependent block of Na+ channels by local anesthetics. *Science* 265(5179):1724-1728.
11. Gilchrist J, Olivera BM, & Bosmans F (2014) Animal toxins influence voltage-gated sodium channel function. *Handb Exp Pharmacol* 221:203-229.
12. French RJ, Yoshikami D, Sheets MF, & Olivera BM (2010) The tetrodotoxin receptor of voltage-gated sodium channels--perspectives from interactions with micro-conotoxins. *Mar Drugs* 8(7):2153-2161.
13. Zhang MM, *et al.* (2007) Structure/function characterization of micro-conotoxin KIIIA, an analgesic, nearly irreversible blocker of mammalian neuronal sodium channels. *J Biol Chem* 282(42):30699-30706.
14. Khoo KK, *et al.* (2012) Distinct disulfide isomers of mu-conotoxins KIIIA and KIIIB block voltage-gated sodium channels. *Biochemistry* 51(49):9826-9835.
15. McArthur JR, *et al.* (2011) Interactions of key charged residues contributing to selective block of neuronal sodium channels by mu-conotoxin KIIIA. *Mol Pharmacol* 80(4):573-584.
16. Zhang MM, *et al.* (2009) Synergistic and antagonistic interactions between tetrodotoxin and mu-conotoxin in blocking voltage-gated sodium channels. *Channels (Austin)* 3(1):32-38.
17. Korkosh VS, Zhorov BS, & Tikhonov DB (2014) Folding similarity of the outer pore region in prokaryotic and eukaryotic sodium channels revealed by docking of conotoxins

GIIIA, PIIIA, and KIIIA in a NavAb-based model of Nav1.4. *J Gen Physiol* 144(3):231-244.
18. Pan X, *et al.* (2019) Molecular basis for pore blockade of human Na(+) channel Nav1.2 by the mu-conotoxin KIIIA. *Science* 363(6433):1309-1313.
19. Yan Z, *et al.* (2017) Structure of the Nav1.4-beta1 Complex from Electric Eel. *Cell* 170(3):470-482 e411.
20. Song Y, *et al.* (2013) High-resolution comparative modeling with RosettaCM. *Structure* 21(10):1735-1742.
21. Bender BJ, *et al.* (2016) Protocols for Molecular Modeling with Rosetta3 and RosettaScripts. *Biochemistry* 55(34):4748-4763.
22. Gray JJ, *et al.* (2003) Protein-protein docking with simultaneous optimization of rigid-body displacement and side-chain conformations. *J Mol Biol* 331(1):281-299.
23. Wang C, Bradley P, & Baker D (2007) Protein-protein docking with backbone flexibility. *J Mol Biol* 373(2):503-519.
24. Kubota T, *et al.* (2017) Mapping of voltage sensor positions in resting and inactivated mammalian sodium channels by LRET. *Proc Natl Acad Sci U S A* 114(10):E1857-E1865.
25. Shen H, Liu D, Wu K, Lei J, & Yan N (2019) Structures of human Nav1.7 channel in complex with auxiliary subunits and animal toxins. *Science*.
26. Shen H, *et al.* (2018) Structural basis for the modulation of voltage-gated sodium channels by animal toxins. *Science*.
27. Payandeh J, Scheuer T, Zheng N, & Catterall WA (2011) The crystal structure of a voltage-gated sodium channel. *Nature* 475(7356):353-358.
28. Kimball IH, Nguyen PT, Sack JT, & Yarov-Yarovoy V (2016) Mapping the Nav1.7 Channel Interaction with the Conotoxin KIIIA. *Biophysical Journal* 110(3):437a-437a.
29. Penzotti JL, Fozzard HA, Lipkind GM, & Dudley SC, Jr. (1998) Differences in saxitoxin and tetrodotoxin binding revealed by mutagenesis of the Na+ channel outer vestibule. *Biophys J* 75(6):2647-2657.
30. Hidalgo P & MacKinnon R (1995) Revealing the architecture of a K+ channel pore through mutant cycles with a peptide inhibitor. *Science* 268(5208):307-310.
31. Pan X, *et al.* (2019) Molecular basis for pore blockade of human Na(+) channel Nav1.2 by the mu-conotoxin KIIIA. *Science*.
32. Pan X, *et al.* (2018) Structure of the human voltage-gated sodium channel Nav1.4 in complex with beta1. *Science*.
33. Silva DA, *et al.* (2019) De novo design of potent and selective mimics of IL-2 and IL-15. *Nature* 565(7738):186-191.
34. Hosseinzadeh P, *et al.* (2017) Comprehensive computational design of ordered peptide macrocycles. *Science* 358(6369):1461-1466.
35. Bhardwaj G, *et al.* (2016) Accurate de novo design of hyperstable constrained peptides. *Nature* 538(7625):329-335.
36. Shaw DE, *et al.* (2014) Anton 2: Raising the bar for performance and programmability in a special-purpose molecular dynamics supercomputer. *Sc14: International Conference for High Performance Computing, Networking, Storage and Analysis*:41-53.
37. Wang RY, *et al.* (2016) Automated structure refinement of macromolecular assemblies from cryo-EM maps using Rosetta. *Elife* 5.
38. Bonneau R, *et al.* (2002) De novo prediction of three-dimensional structures for major protein families. *J Mol Biol* 322(1):65-78.

39. Fleishman SJ, *et al.* (2011) RosettaScripts: a scripting language interface to the Rosetta macromolecular modeling suite. *PloS one* 6(6):e20161.
40. Jo S, Kim T, Iyer VG, & Im W (2008) CHARMM-GUI: a web-based graphical user interface for CHARMM. *J Comput Chem* 29(11):1859-1865.
41. Jiang W, *et al.* (2011) High-performance scalable molecular dynamics simulations of a polarizable force field based on classical Drude oscillators in NAMD. *J Phys Chem Lett* 2(2):87-92.
42. Gasteiger E, *et al.* (2005) Protein Identification and Analysis Tools on the ExPASy Server;. *The Proteomics Protocols Handbook*, ed Walker JM (Humana Press), pp 571-607.

Figure 1

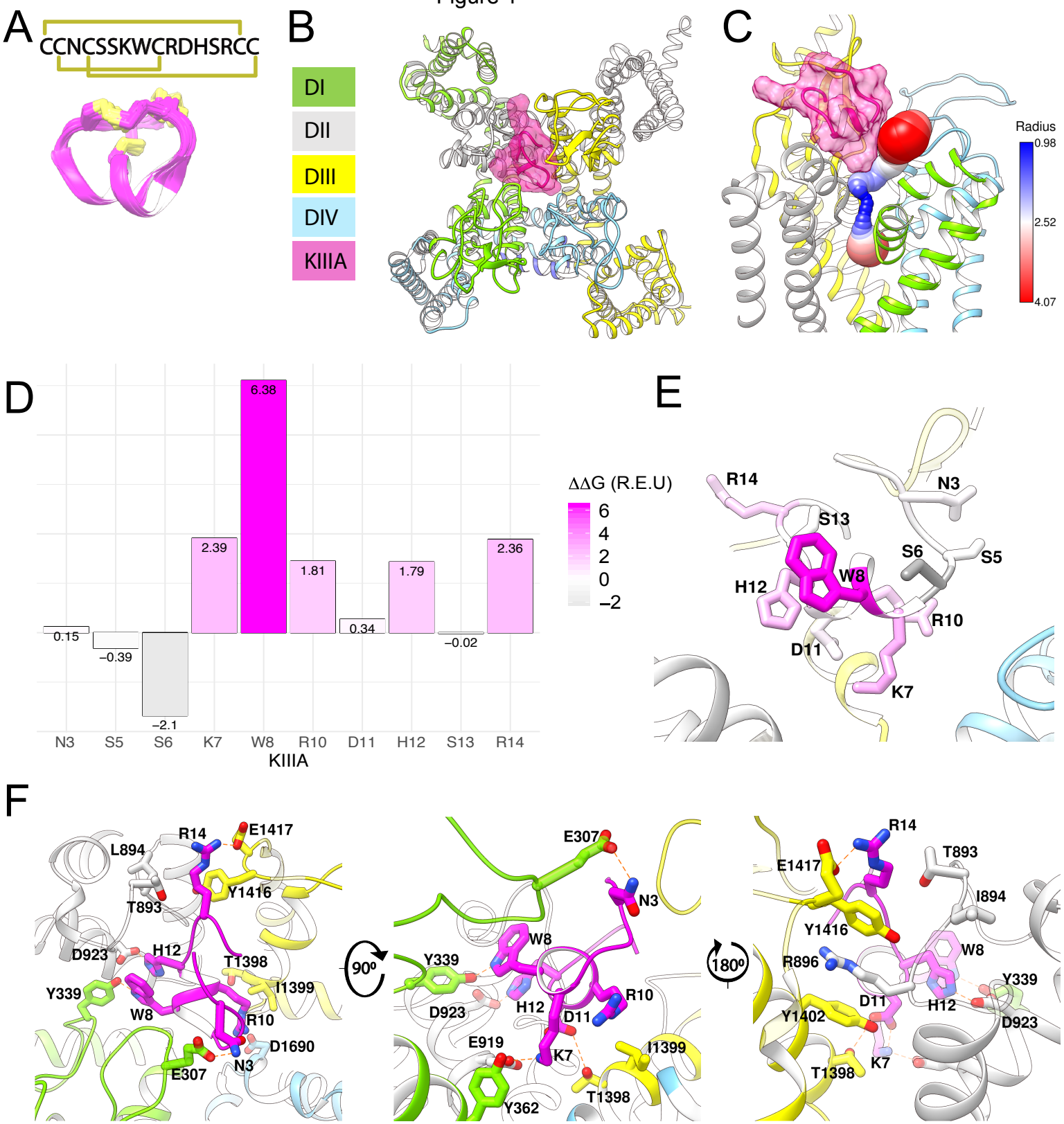
A
CCNCSSKWCRDHSRCC
B
DI
DII
DIII
DIV
KIIIA
C
Radius
0.98
2.52
4.07
D
6.38
2.39
1.81
1.79
2.36
0.15
−0.39
−2.1
0.34
−0.02
N3
S5
S6
K7
W8
R10
D11
H12
S13
R14
KIIIA
ΔΔG (R.E.U)
6
4
2
0
−2
E
R14
N3
S13
S6
S5
H12
W8
R10
D11
K7
F
R14
E1417
L894
T893
Y1416
D923
H12
T1398
I1399
Y339
W8
R10
D1690
E307
N3
90º
E307
N3
W8
Y339
D923
H12
D11
R10
E919
K7
I1399
Y362
T1398
180º
R14
T893
E1417
I894
Y1416
W8
R896
Y339
D11
H12
Y1402
D923
T1398
K7

Figure 2

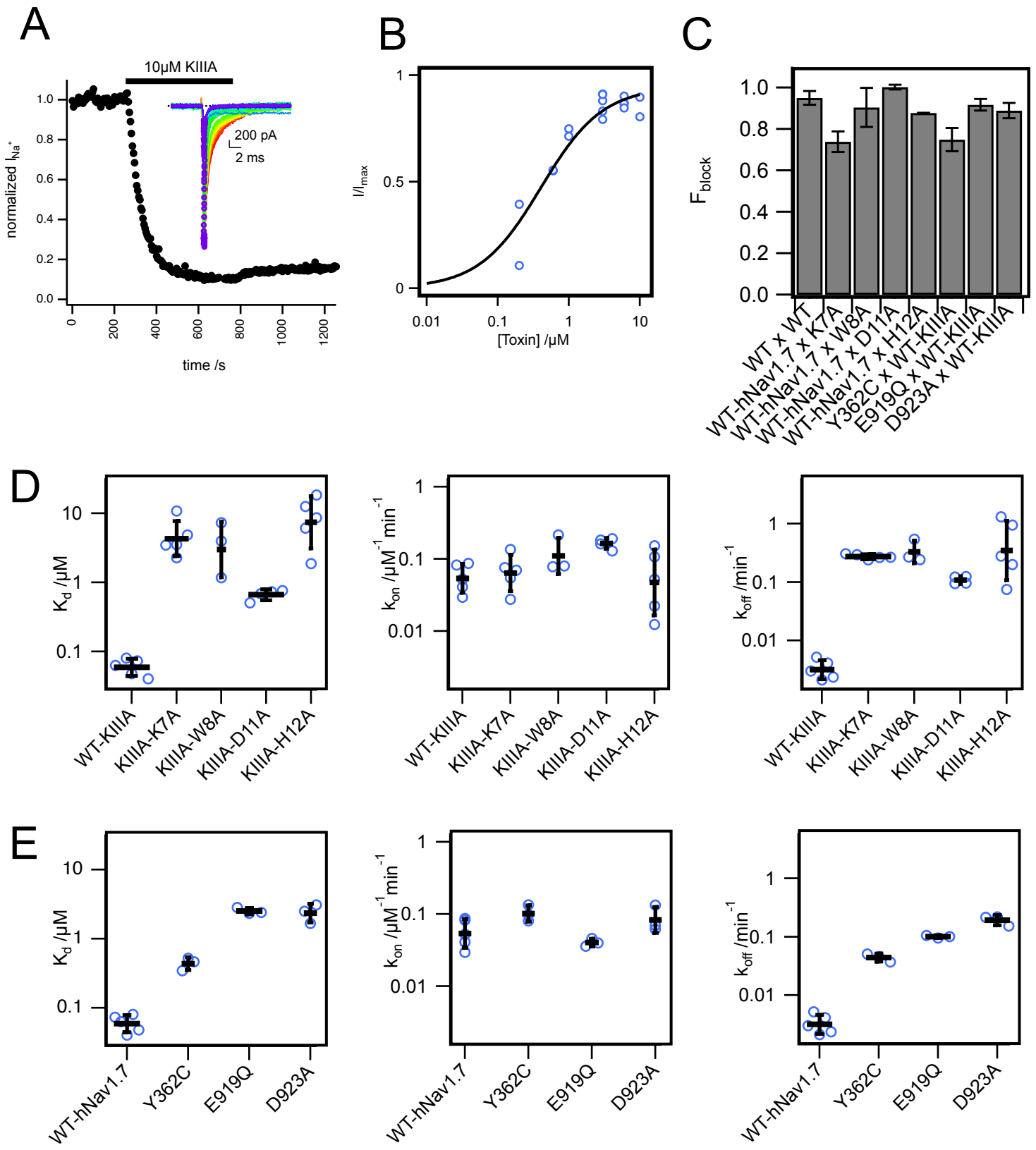
A
10μM KIIIA
normalized I_{Na^+}
200 pA
2 ms
time /s
B
I/I_{max}
[Toxin] /μM
C
F_{block}
WT x WT
WT-hNav1.7 x K7A
WT-hNav1.7 x W8A
WT-hNav1.7 x D11A
WT-hNav1.7 x H12A
Y362C x WT-KIIIA
E919Q x WT-KIIIA
D923A x WT-KIIIA
D
K_d /μM
k_{on} /μM^{-1} min^{-1}
k_{off} /min^{-1}
WT-KIIIA
KIIIA-K7A
KIIIA-W8A
KIIIA-D11A
KIIIA-H12A
E
WT-hNav1.7
Y362C
E919Q
D923A

Figure 3

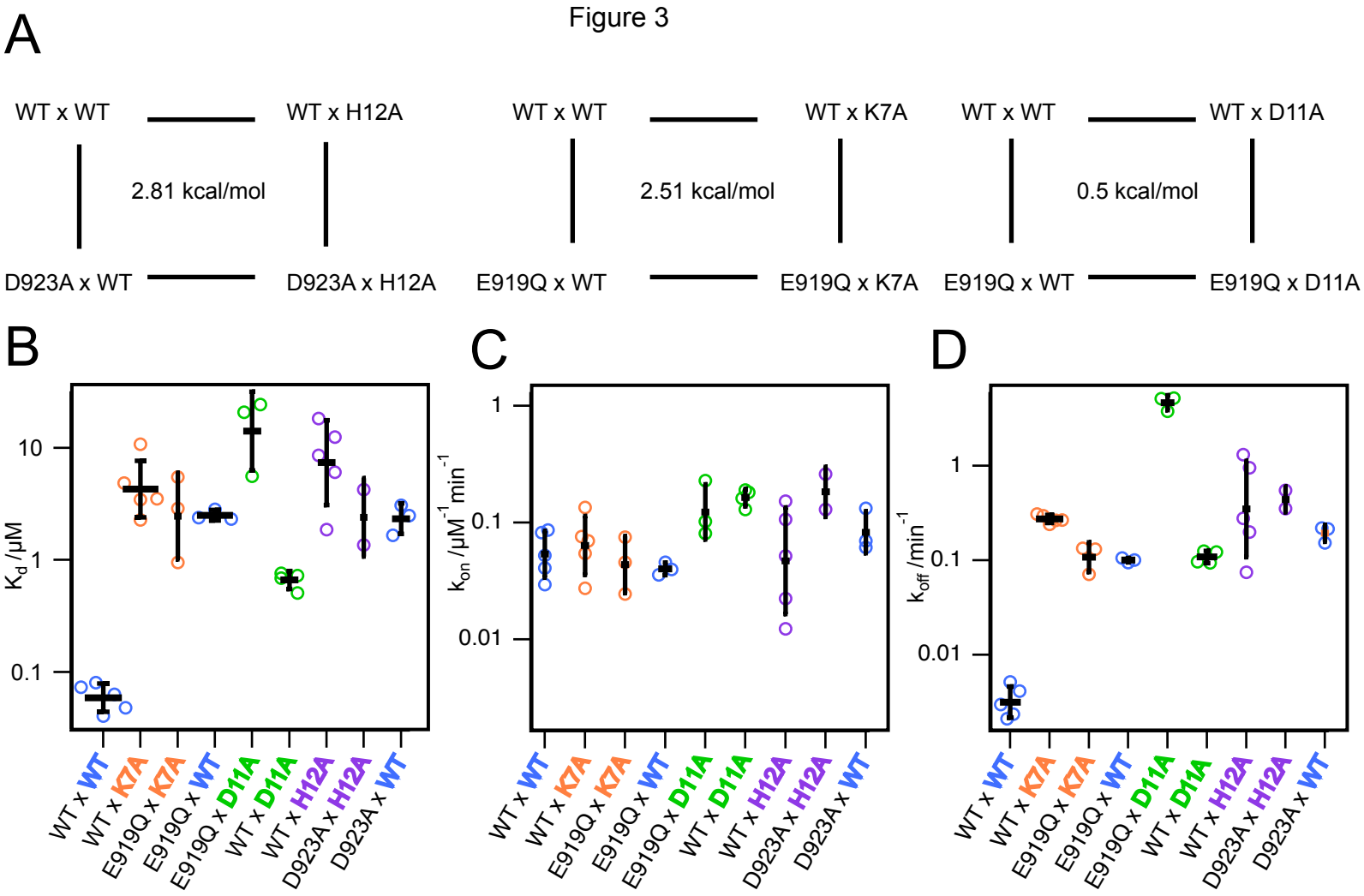
A
WT x WT
WT x H12A
2.81 kcal/mol
D923A x WT
D923A x H12A
WT x WT
WT x K7A
2.51 kcal/mol
E919Q x WT
E919Q x K7A
WT x WT
WT x D11A
0.5 kcal/mol
E919Q x WT
E919Q x D11A
B
C
D
K_d /μM
k_{on} /μM^{-1}min^{-1}
k_{off} /min^{-1}
10
1
0.1
0.01
WT x WT
WT x K7A
E919Q x K7A
E919Q x WT
E919Q x D11A
WT x D11A
WT x H12A
D923A x H12A
D923A x WT

Figure 4

A

DI | DII | DIII | DIV | KIIIA | hNav1.2 | KIIIA(hNav1.2)

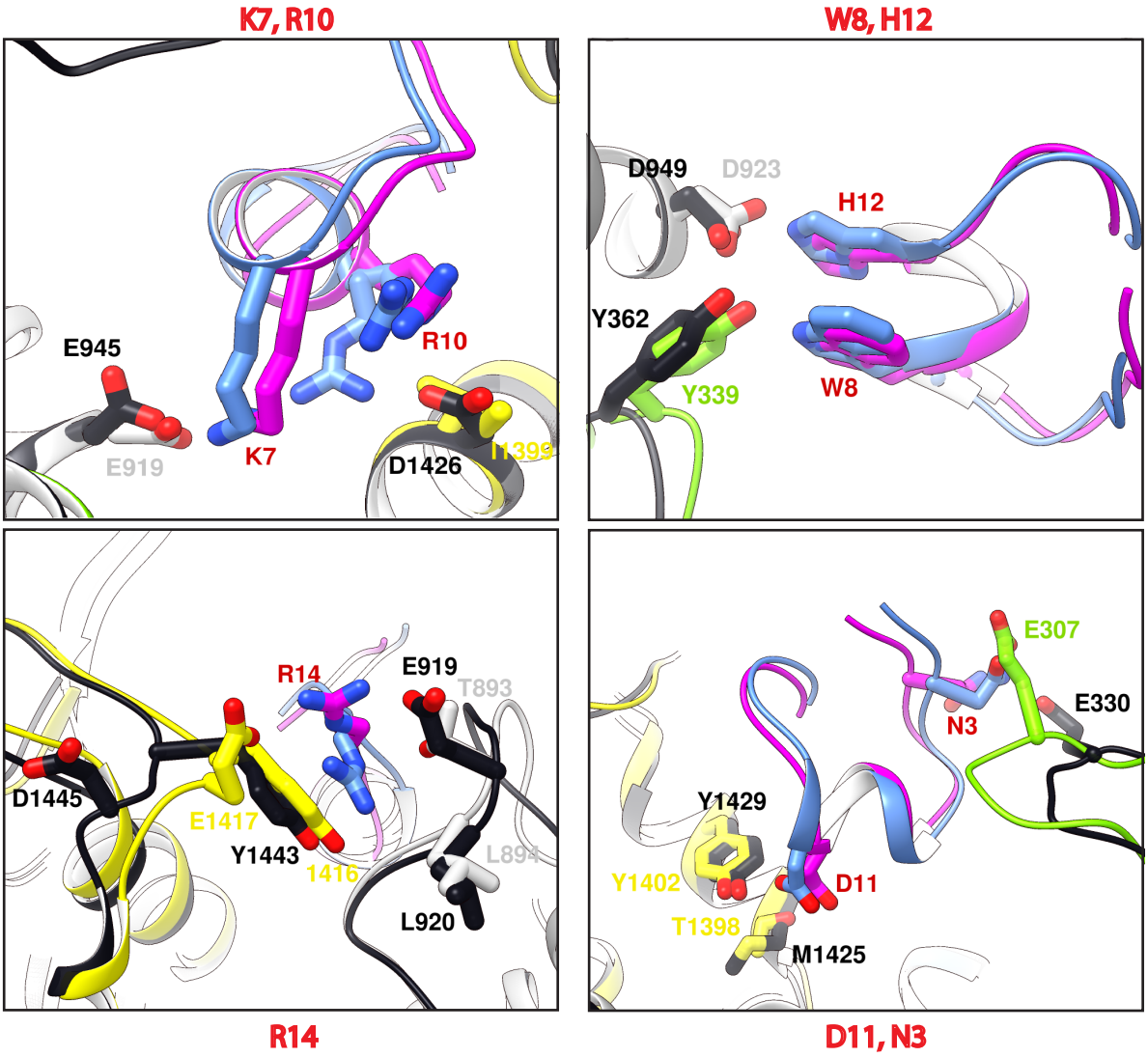

B

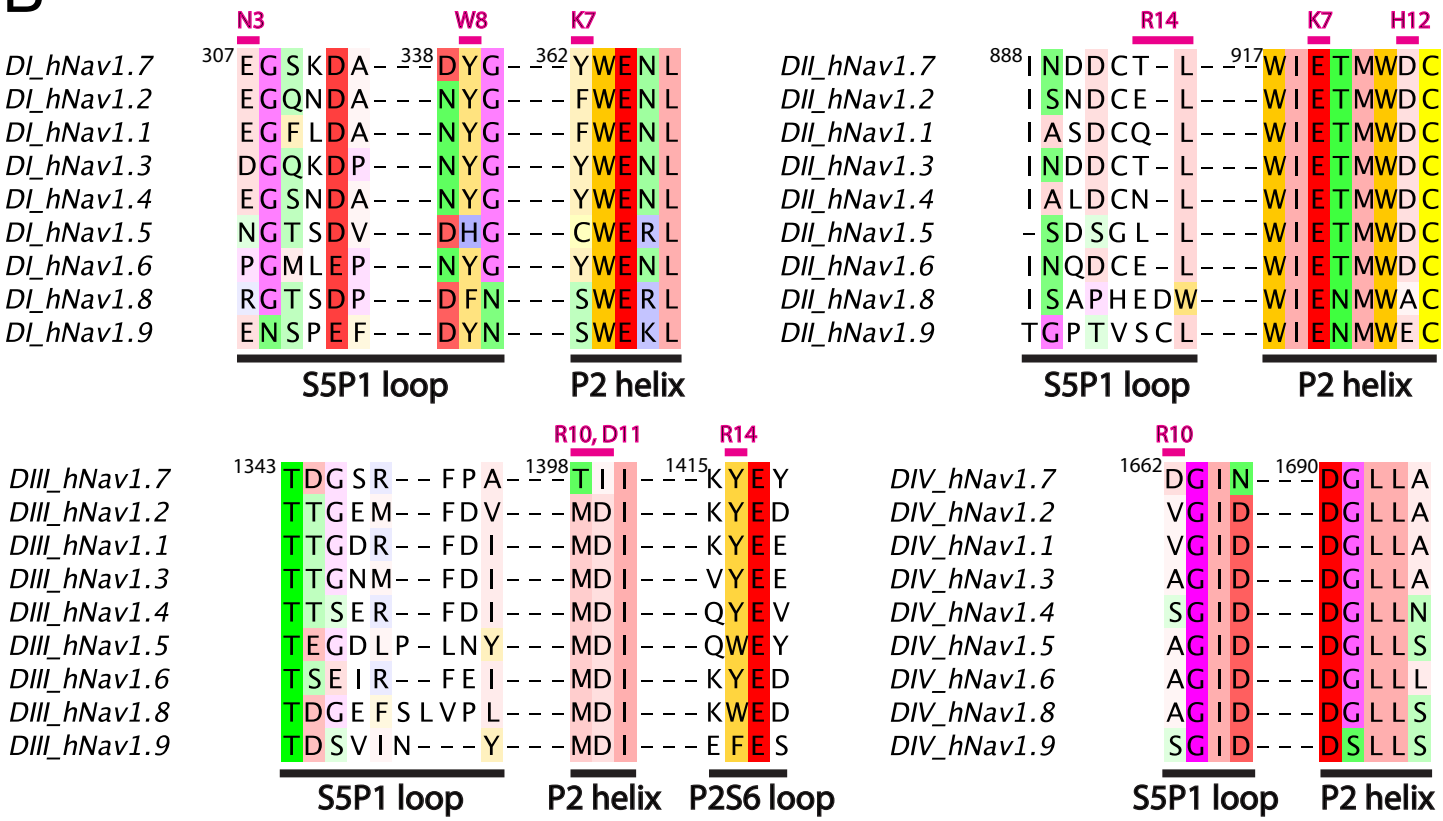

Figure 5

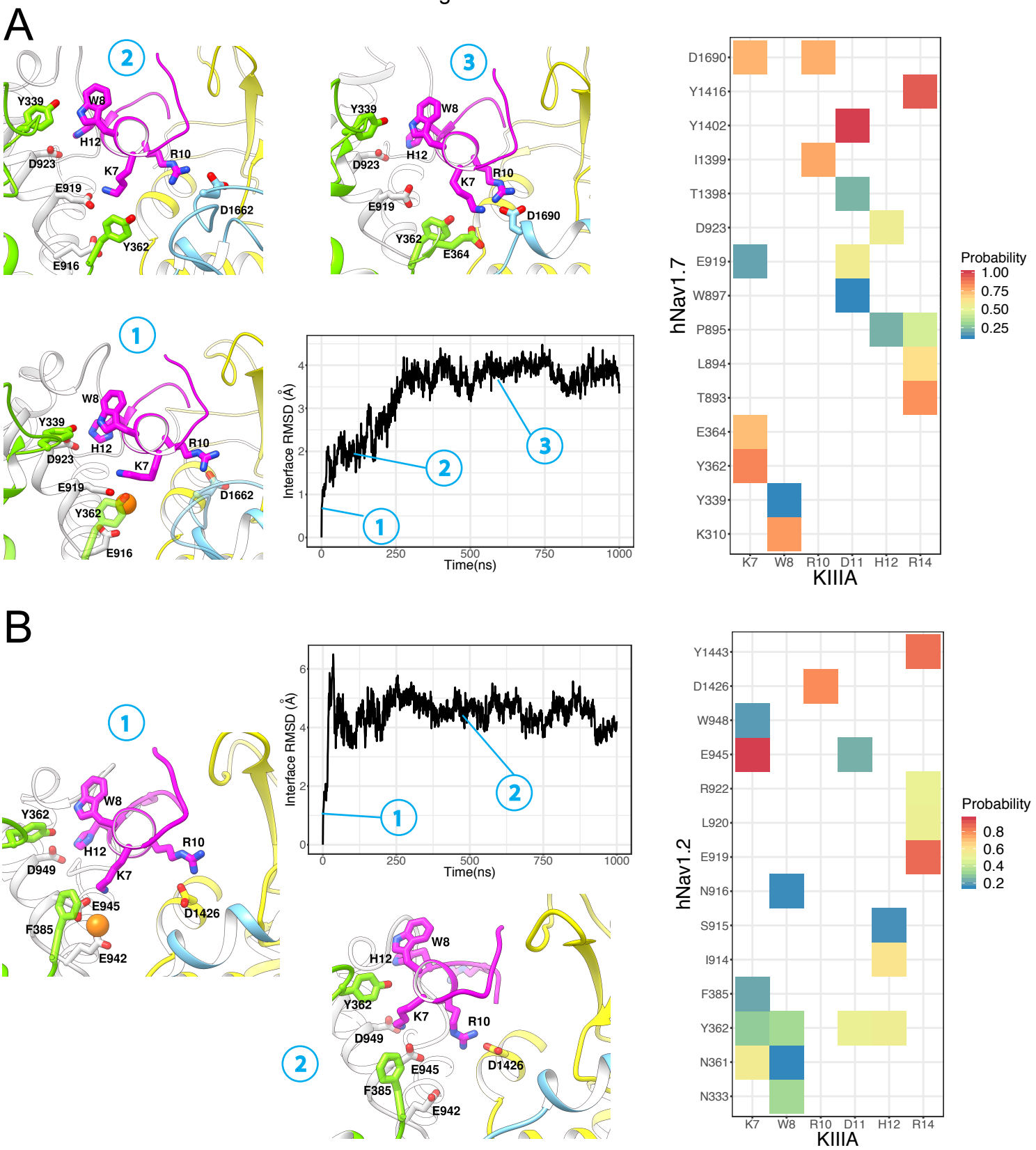
A
2
Y339
W8
H12
R10
D923
K7
E919
D1662
Y362
E916
3
Y339
W8
H12
D923
R10
K7
E919
D1690
Y362
E364
1
W8
Y339
H12
R10
D923
K7
E919
D1662
Y362
E916
Interface RMSD (Å)
Time(ns)
0
250
500
750
1000
hNav1.7
D1690
Y1416
Y1402
I1399
T1398
D923
E919
W897
P895
L894
T893
E364
Y362
Y339
K310
K7
W8
R10
D11
H12
R14
KIIIA
Probability
1.00
0.75
0.50
0.25
B
1
W8
Y362
H12
R10
D949
K7
E945
D1426
F385
E942
Interface RMSD (Å)
Time(ns)
0
250
500
750
1000
2
W8
H12
Y362
K7
R10
D949
E945
D1426
F385
E942
hNav1.2
Y1443
D1426
W948
E945
R922
L920
E919
N916
S915
I914
F385
Y362
N361
N333
K7
W8
R10
D11
H12
R14
KIIIA
Probability
0.8
0.6
0.4
0.2